INORGANIC CHEMISTRY FRONTIERS

RESEARCH ARTICLE

View Article Online
View Journal | View Issue

Cite this: *Inorg. Chem. Front.*, 2025, **12**, 3469

Rare earth double perovskites for underwater X-ray imaging applications†

Ying Wang,‡[a,b] Chao Wang,‡[b] Luxuan Men,[b] Jinlong Zhu,[b] Qingsong Hu,*[a,c] Jiawen Xiao *[b] and Omar F. Mohammed *[c]

Received 25th December 2024,
Accepted 6th March 2025

DOI: 10.1039/d4qi03325f

rsc.li/frontiers-inorganic

Lanthanide metal halide double perovskites (Ln-MHDPs) are promising scintillator materials due to their outstanding luminescence properties and high X-ray absorption cross-sections. With the growing demand for advanced X-ray imaging scintillators, there is increasing interest in the exploration of new scintillation materials suitable for novel applications under harsh conditions. In this study, we present a series of Ln-MHDPs with tunable fluorescence emission spanning the visible and near-infrared regions, effectively activated by both ultraviolet and X-ray excitation. The $Cs_2NaLnCl_6$ (Ln = Eu, Tb, Ho, Er, and Yb) compounds demonstrated high X-ray sensitivity, excellent stability, and low detection limits under X-ray irradiation. Notably, $Cs_2NaTbCl_6$ exhibited a light yield of 42 200 photons per MeV, while retaining 98% of its initial radioluminescence intensity after 180 minutes of X-ray exposure, corresponding to a total radiation dose of approximately 86.4 Gy. Moreover, these materials achieved a spatial resolution of 10 lp mm^{-1}, even in flexible forms. The application of polydimethylsiloxane coating significantly enhanced the water resistance of the $Cs_2NaLnCl_6$ compounds and facilitated clear underwater X-ray imaging. This study highlights the promising potential of Ln-MHDPs for underwater X-ray imaging applications.

1. Introduction

Scintillators are widely employed in high-energy physics, security inspection, medical imaging, aerospace, and oil exploration.[1–5] Indirect imaging scintillators currently dominate the market for X-ray imaging technologies due to their low raw material cost, high detection efficiency, and excellent stability.[3] However, traditional inorganic scintillators face limitations such as complex manufacturing processes, low light yield (LY), poor mechanical properties, and extreme moisture sensitivity.[6–8] While organic scintillators are promising, they suffer from inferior X-ray absorption capacity due to the predominance of light elements with very low X-ray absorption cross-sections.[9–11] In recent years, $CsPbX_3$ (X = Cl, Br, and I) has emerged as a promising next-generation scintillator, offering a high X-ray attenuation coefficient, excellent emission properties, and a tunable bandgap.[12,13] However, its intrinsic instability and lead toxicity hinder commercial applications.[14–16] In addition, imaging detectors paired with scintillators require higher doses, posing risks to human health.[17,18] Furthermore, rigid scintillators are prone to anamorphosis, which reduces image quality and can cause operational failure after bending.[18–22] Addressing these challenges necessitates the development of scintillators that are easy to manufacture, environmentally friendly, and highly bright, sensitive, and adaptable to extreme and complex environments, thereby leading to the advancement of X-ray imaging technologies.

Rare earth elements (REs) are often referred to as the "vitamins" in light functional materials due to their numerous energy levels and over 20 000 electronic transitions, which highlight their importance in luminescence.[23–25] In this context, the high X-ray absorption efficiency, versatility in preparation methods, natural abundance, and eco-friendliness of REs notably contribute to their development in scintillator technology.[26] Newly developed RE-based metal halide scintillators effectively overcome the limitations of traditional inorganic and organic scintillators.[20,26] However, the synthesis protocols for these RE-based halide scintillators remain unclear, and the relationship between their optical properties and chemical structure is not fully understood.[27,28] In addition, their extreme sensitivity to water greatly limits their practical applications.

[a]*Hubei Key Laboratory of Low Dimensional Optoelectronic Materials and Devices, Institute of Functional Materials, Hubei University of Arts and Science, Xiangyang 441053, China. E-mail: qingsong.hu@kaust.edu.sa*
[b]*Beijing Key Lab of Microstructure and Property of Advanced Materials, College of Materials Science and Engineering, Beijing University of Technology, Beijing 100124, China. E-mail: xiaojw@bjut.edu.cn*
[c]*Center for Renewable Energy and Storage Technologies (CREST), Division of Physical Sciences and Engineering, King Abdullah University of Science and Technology (KAUST), Thuwal 23955-6900, Kingdom of Saudi Arabia. E-mail: omar.abdelsaboor@kaust.edu.sa*

†Electronic supplementary information (ESI) available. See DOI: https://doi.org/10.1039/d4qi03325f

‡These authors contributed equally to this work.

Research studies on new RE-based nanocrystals (NCs) and bulk materials have mainly focused on light emitting diodes and anticounterfeiting applications, with limited attention being given to unlocking their potential in scintillator technology.[29–33]

In this study, we successfully fabricated a series of RE $Cs_2NaLnCl_6$ scintillators using the hydrothermal method. We systematically investigated the spectral characteristics and luminescence mechanisms of these photoluminescent materials and identified several promising candidates for further study of their scintillation properties. $Cs_2NaHoCl_6$, $Cs_2NaYbCl_6$, and $Cs_2NaTmCl_6$ exhibited light yields (LYs) of 9600, 6000, and 1300 photons per MeV, respectively. Remarkably, $Cs_2NaTbCl_6$ achieved a record-high photoluminescence quantum yield (PLQY) of 85%, highlighting its potential for X-ray imaging applications. The potential of lanthanide metal halide double perovskites (Ln-MHDPs) for X-ray imaging is further emphasized by their ability to produce high-contrast images and their high sensitivity for various objects. We also prepared and tested several flexible scintillation screens for X-ray imaging applications. Our results demonstrate that these screens have a tensile strength of up to 180% and maintain their integrity after repeated stress applications. Compared with traditional rigid scintillation screens, flexible screens significantly reduce the anamorphism and image halo effects when imaging curved objects. Furthermore, our use of a polymer film proved effective for stable underwater X-ray imaging. These flexible scintillation screens are particularly well-suited to extreme conditions, advancing the development of high-performance flexible X-ray detectors.

2. Results and discussion

2.1 Synthesis and crystal phase of Ln-MHDPs

Ln-MHDP polycrystals were synthesized using a modified solvothermal approach, and a schematic of the synthesis is shown in Fig. 1(a). The solvothermal process effectively controlled the reaction conditions and crystal growth through factors such as temperature, pressure, and reaction time. The polycrystals of $Cs_2NaLnCl_6$ (Ln = Eu, Tb, Ho, Er, Tm, Yb, Sc, Y, and Lu) are shown in Fig. S1.† The powder X-ray diffraction (XRD) patterns of $Cs_2NaLnCl_6$ for all Ln metal ions revealed a cubic crystal phase (space group: *Fm*3*m*), with no impurities detected, aligning well with the standard card data of $Cs_2NaErCl_6$ (PDF#89-0053) (Fig. 1b and S2†). The diffraction peaks consistently shift to higher 2θ angles as the lanthanide series progresses from La to Yb, as shown in the enlarged XRD region of 2θ = 23°–24° in Fig. 1(b). This phenomenon, known as the lanthanide contraction effect, is attributed to the gradual decrease in the ionic radius from 0.106 nm for La^{3+} to 0.085 nm for Lu^{3+} with increasing atomic number. The corresponding lattice parameters for each $Cs_2NaLnCl_6$ material obtained from the Materials Project crystal structure database show a reduction from 11.16 Å for $Cs_2NaLaCl_6$ to 10.82 Å for $Cs_2NaLuCl_6$. The linear relationship between these lattice parameters and the corresponding Ln^{3+} cation radius, as shown in Fig. 1(c), indicates that the lattice shrinkage is primarily due to the decrease in the size of the Ln^{3+} ions. The cell parameters of $Cs_2NaYbCl_6$ were not available in the Materials Project database; thus, the relationship between its lattice constants and Yb^{3+} ion radius is not included in Fig. 1(c).

Field emission scanning electron microscopy (FESEM) was used to observe the microscopic morphology. The FESEM images of $Cs_2NaEuCl_6$ shown in Fig. S3(a)† revealed micron-sized particles, some of which exhibit agglomeration. This agglomeration could be mitigated by ball milling following ethanol recleaning. Energy-dispersive spectroscopy (EDS) elemental analysis further confirmed the chemical composition, with the images in Fig. S3(a)† demonstrating a uniform distribution of Cs, Na, Eu, and Cl in $Cs_2NaEuCl_6$. The semi-quantitative atomic proportions of 21.73%, 11.50%, 10.79%, and 55.98%, as shown in Table S1,† are closely aligned with the standard stoichiometric ratio of the compound, thereby

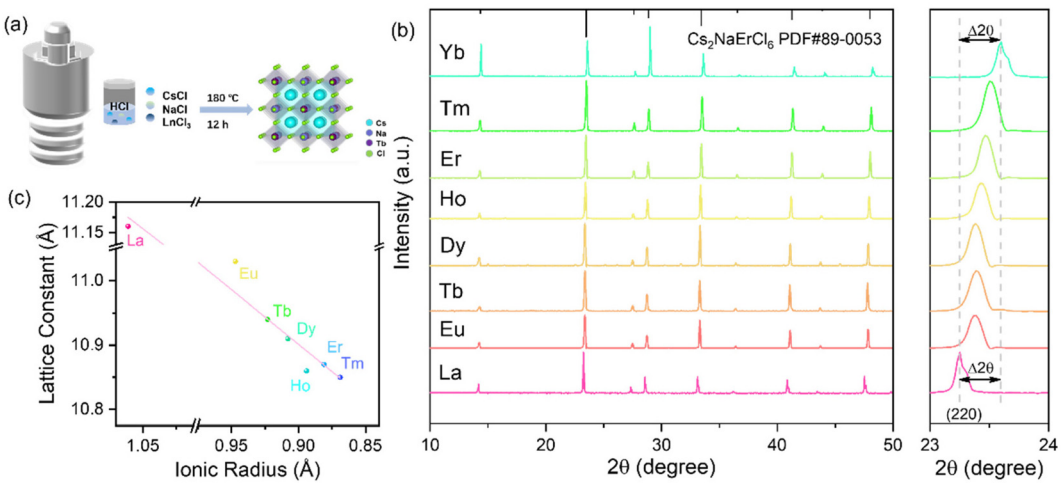

Fig. 1 (a) Schematic illustration of the Ln-MHDP synthesis process. (b) XRD patterns of $Cs_2NaLnCl_6$ (Ln = La, Eu, Tb, Dy, Ho, Er, Tm, and Yb) powders. The enlarged XRD pattern of the 2θ = 23°–24° region is shown on the right. (c) The linear correlation (R^2 = 0.92) between the size of the rare earth ion and the experimentally determined lattice constants of $Cs_2NaLnCl_6$.

validating its phase purity. Further FESEM and EDS analyses were conducted on additional samples, as illustrated in Fig. S3 and S4.† Table S1† summarizes the atomic proportions of the synthesized samples. The results show that the atomic proportions of Cs, Na, and Ln are approximately consistent with the expected values of corresponding double perovskites except for the slightly lower proportions of Cl. The possible reason is that the Cl element is very sensitive to electron beams and is easily destroyed by electron beam irradiation during EDS characterization, resulting in Cl defects on the surface of the materials. These results support the successful synthesis of high-purity $Cs_2NaLnCl_6$.

2.2 Optical properties of Ln-MHDPs

After identifying the structure, we selected $Cs_2NaLnCl_6$ (Ln = Eu, Tb, Ho, Er, Tm, and Yb) to investigate its PL properties. The crystals were photographed during daylight hours and under ultraviolet (UV) light. As shown in Fig. S1,† $Cs_2NaEuCl_6$, $Cs_2NaHoCl_6$, $Cs_2NaErCl_6$, $Cs_2NaTmCl_6$, $Cs_2NaScCl_6$, and Cs_2NaYCl_6 are light yellow transparent crystals under daylight, and $Cs_2NaTbCl_6$, $Cs_2NaYbCl_6$, and $Cs_2NaLuCl_6$ appear as colorless transparent crystals. This is because different materials absorb visible light differently, and the color of the material seen by the human eye comes from the part of the sunlight reflected by the material. Under UV irradiation, $Cs_2NaScCl_6$, Cs_2NaYCl_6, and $Cs_2NaLuCl_6$ emit blue light, while $Cs_2NaEuCl_6$, $Cs_2NaTbCl_6$, $Cs_2NaHoCl_6$, and $Cs_2NaErCl_6$ emit red, green, red, and blue-green light, respectively. The emission colors from $Cs_2NaTmCl_6$ and $Cs_2NaYbCl_6$ are invisible to the naked eye as they emit near-infrared (NIR) light. According to the spectral test results, six of the synthesized Ln-MHDPs, $Cs_2NaLnCl_6$ (Ln = Eu, Tb, Ho, Er, Tm, and Yb), exhibited notable emission colors with PL peaks spanning a wide range, from visible (Ln = Eu, Tb, Ho, and Er) to NIR (Ln = Er, Tm, and Yb), as shown in Fig. 2(a). The characteristic excitation and emission spectra of each material are exhibited. The excitation and emission of trivalent RE ions (except Ce^{3+}) arise from transitions involving 4f–4f electrons, resulting in sharp, narrow peaks.[34] These materials exhibit relatively long lifetimes, on the order of milliseconds, due to the f–f transitions, as depicted in Fig. 2(c–h). The emission and excitation peaks and lifetimes of $Cs_2NaLnCl_6$ (Ln = Eu, Tb, Ho, Er, Tm, and Yb) are summarized in Table S2.† The photoluminescence excitation (PLE), PL, and lifetimes of $Cs_2NaLnCl_6$ (Ln = Sc, Y, and Lu) were studied, as shown in Fig. S5.† These materials, which emit from the self-trapped exciton radiative recombination with LYs below 2000 photons per MeV, are thus not discussed further.

Under excitation at 394 nm, $Cs_2NaEuCl_6$ exhibits intense red emission peaks at 592 and 614 nm, originating from the $^5D_0 \rightarrow {}^7F_J$ (J = 1 and 2) transitions of Eu^{3+}, along with weaker transitions observed at 652 nm ($^5D_0 \rightarrow {}^7F_3$) and 704 nm ($^5D_0 \rightarrow {}^7F_4$), as depicted in Fig. 2(b). The peak at 592 nm ($^5D_0 \rightarrow {}^7F_1$) results from a magnetic dipole transition, while the peak at 614 nm ($^5D_0 \rightarrow {}^7F_2$) is attributed to an electric dipole transition.[29,35] The emission at 614 nm exhibits a long lifetime of 2.61 ms due to the spin-forbidden nature of the f–f relaxation pathways. The photoluminescence quantum yield (PLQY) of the sample was found to be approximately 5%. This low PLQY can be primarily attributed to the high concentration of Eu^{3+}, which leads to concentration quenching, enhancing non-radiative relaxation, and thereby greatly reducing the material's PLQY.[36]

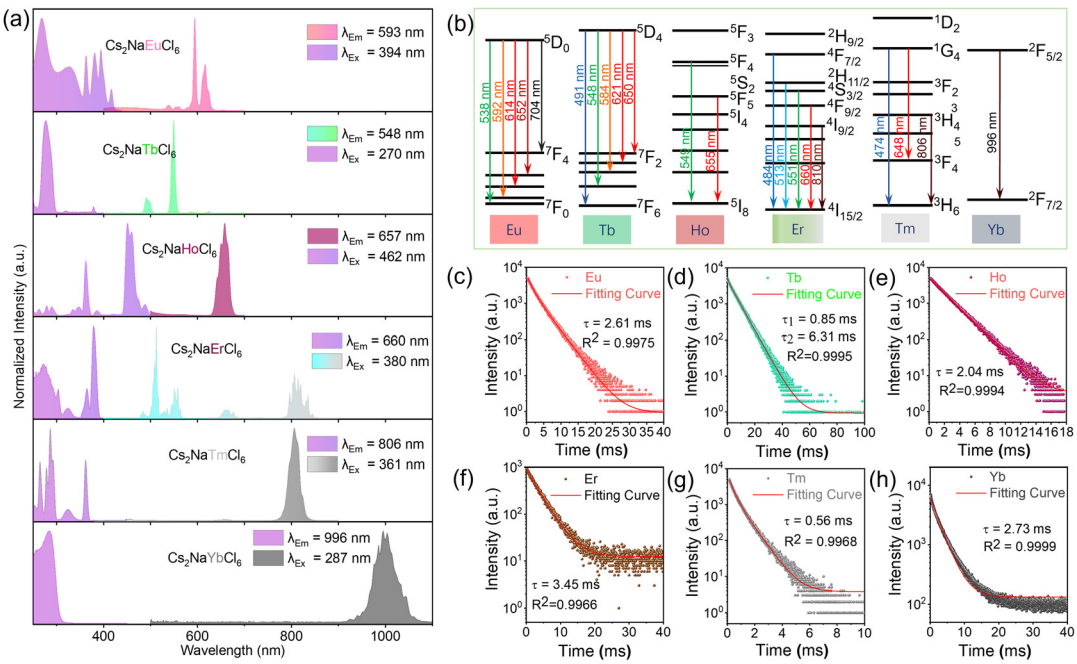

Fig. 2 (a) Photoluminescence excitation (PLE) spectra and PL spectra of $Cs_2NaLnCl_6$ (Ln = Eu, Tb, Ho, Er, Tm, Yb). (b) Energy level diagrams of the emission spectra from the six discussed Ln-MHDPs. (c–h) PL lifetime decay plots and fitted curves of the six discussed Ln-MHDPs.

In contrast, $Cs_2NaTbCl_6$ demonstrates a strong green emission originating from the Tb $^5D_4 \rightarrow {}^7F_J$ (J = 2–6) transitions, with the most intense peak observed at 548 nm (Fig. 2a). The observed emissive transitions are sensitized by a strong, sharp 4f → 5d absorption feature at 270 nm, as shown in the PLE spectrum.[37] Notably, $Cs_2NaTbCl_6$ exhibited a two-component lifetime, τ_1 = 0.85 ms and τ_2 = 6.31 ms, corresponding to the $^5D_4$ excited state, which is in good agreement with previously reported values in the literature.[35] The shorter lifetime component may be attributed to crystal defect-induced nonradiative channels.[35] Furthermore, $Cs_2NaTbCl_6$ achieved a high PLQY of 86%, the highest value reported to date among Ln-MHDPs. This exceptional PLQY is likely due to the reduced probability of nonradiative relaxation processes, attributed to the relatively discrete ground-state levels of Tb^{3+} (^7F_J [J = 2–6]).

The highest excitation peak of $Cs_2NaHoCl_6$ at approximately 450 nm, with a corresponding emission peak at 655 nm, can be attributed to the $^5F_5 \rightarrow {}^5I_8$ transition.[38] Typically, emissions from the $^5F_4 \rightarrow {}^5I_8$ and $^5F_5 \rightarrow {}^5I_8$ transitions of Ho^{3+} occur simultaneously and are prominent; however, a competitive relationship exists between these transitions.[39] In $Cs_2NaHoCl_6$, the emission from the $^5F_4 \rightarrow {}^5I_8$ transition is entirely suppressed, leaving only a strong emission from the $^5F_5 \rightarrow {}^5I_8$ transition. This observation highlights the need for further investigation into the relationship between material structure and luminescence characteristics, which could guide the development of new luminescent materials.

Upon excitation at 380 nm UV light, $Cs_2NaErCl_6$ exhibited emission colors spanning green, yellow, red, and the NIR regions, corresponding to the $^2H_{11/2}$, $^4S_{3/2} \rightarrow {}^4I_{15/2}$, $^4F_{9/2} \rightarrow {}^4I_{15/2}$, and $^4I_{9/2} \rightarrow {}^4I_{15/2}$ electronic transitions, respectively.[40,41] The fluorescence lifetime at 660 nm emission was measured at 3.45 ms. $Cs_2NaTmCl_6$ predominantly emits at 806 nm when excited by 361 nm UV light, deviating from the typical Tm^{3+} blue light emission ($^1G_4 \rightarrow {}^3H_6$).[42,43] Meanwhile, $Cs_2NaYbCl_6$ exhibits a weak Yb^{3+} emission feature at 996 nm, consistent with other Yb-containing perovskites.[37] The observed PL lifetime of 2.73 ms exceeds the 47.5 μs reported for $Cs_2NaYbCl_6$ NCs and the 475 μs reported for Yb-doped $CsPbCl_3$ perovskite NCs.[37,44] The shorter lifetimes reported in the literature are attributed to PL quenching caused by Yb–Yb coupling.[44] However, the PL lifetime of our polycrystals surpasses that of NCs, despite the higher concentration of Yb in $Cs_2NaYbCl_6$. This suggests that vibrational relaxation or other nonradiative recombination mechanisms, rather than Yb–Yb coupling, are more likely responsible for the reduced fluorescence lifetime in Yb^{3+} NCs.[44] These mechanisms contribute to weak Yb^{3+} emission in RE NCs but are effectively mitigated in polycrystals, resulting in considerably enhanced radiative recombination.

2.3 Radioluminescence (RL) properties

Fig. 3(a) and S6† show the radioluminescence (RL) spectra of $Cs_2NaLnCl_6$ (Ln = Eu, Tb, Ho, Er, Tm, Yb, Sc, and Lu). The RL spectra of the selected Ln-MHDPs are similar to their PL spectra, indicating consistency in the recombination paths under UV and X-ray irradiation. Further analysis involved comparing the absorption coefficient of $Cs_2NaLnCl_6$ (Ln = Eu, Tb, Ho, Er, Tm, and Yb) crystals with that of three commercial scintillators: CsI, LYSO, and BGO. The photon energy range is 1–1000 keV, as shown in Fig. 3(b). The data showed that the absorption coefficients of these Ln-MHDPs are comparable to those of the three commercial scintillators.

LY, an essential aspect of scintillator performance, is dependent on X-ray response amplitude and RL spectra. Fig. S6† compares the RL spectra of $Cs_2NaLnCl_6$ under X-ray irradiation with those of LYSO and BGO to determine their LYs. Using a calculation method referenced in the study and LYSO and BGO as standards, the light output of $Cs_2NaLnCl_6$ (Ln = Eu, Tb, Ho, Er, Tm, Yb, Sc, and Lu) was assessed. The method used is detailed in the ESI.† The calculated LYs are summarized in Fig. 3(c) and Table S2.† This analysis compared the RL spectrum of LYSO with that of $Cs_2NaTbCl_6$ (Fig. S6(b)†). The study found that the RL intensity under X-rays for $Cs_2NaTbCl_6$ was significantly higher than that for LYSO. Based on a quantitative comparison of the integral RL intensity, the LY of a $Cs_2NaTbCl_6$ wafer was estimated to be 42 200 photons per MeV, which is slightly lower than that of the single crystal (46 600 photons per MeV) but much higher than that of $Cs_2NaTbCl_6$ NCs (2500 photons per MeV).[14,35] It is noteworthy that the LYs of red $Cs_2NaHoCl_6$ and NIR $Cs_2NaYbCl_6$ and $Cs_2NaTmCl_6$ are reported here for the first time, with test results of 9600, 6000, and 1400 photons per MeV, respectively. However, samples with low LYs do not possess practical application advantages; therefore, subsequent measurements, including stability, linear X-ray response effect, and detection limit, were conducted for samples with an LY value greater than 2000 photons per MeV.

The radiation stability of $Cs_2NaLnCl_6$ (Ln = Eu, Tb, Ho, Er, and Yb) was also investigated under high-dose-rate X-ray irradiation at 8 mGy s^{-1}. After continuous irradiation for 180 min, corresponding to a total radiation dose of ~86.4 Gy, all the samples maintained an irradiation stability of 85%, with $Cs_2NaTbCl_6$ exhibiting the highest stability at 98%, as shown in Fig. 3(d). Notably, the radiation resistance of $Cs_2NaTbCl_6$ considerably over-performed that of CsI:Tl, which retained only 50% stability at 30 Gy, and the double perovskite $Cs_2Ag_{0.6}Na_{0.4}InCl_6$:Bi, which retained only 50% stability at 53 Gy.[45,46] The RL intensity of $Cs_2NaLnCl_6$ (Ln = Eu, Tb, Ho, Er, and Yb) increased linearly with dose rate, as confirmed by Fig. S7,† demonstrating a good linear relationship between the RL intensity and X-ray dose rates ranging from 500 to 6.78 mGy s^{-1}. Given the harmful effects of high radiation doses during exposure to computed tomography (CT) scans, current research focuses on developing scintillators capable of imaging at lower doses. Fig. 3(e) illustrates the detection limit of $Cs_2NaLnCl_6$, which benefits from the narrowband emission of RE ions and their high X-ray response. All measured detection limits were below 300 nGy s^{-1}, with $Cs_2NaTbCl_6$ and $Cs_2NaHoCl_6$ achieving the lowest values of 67.8 and 85.5 nGy s^{-1}, respectively. The LY, stability, and detection limits of $Cs_2NaLnCl_6$ (Ln = Eu, Tb, Ho, Er, Tm, and Yb) are summarized

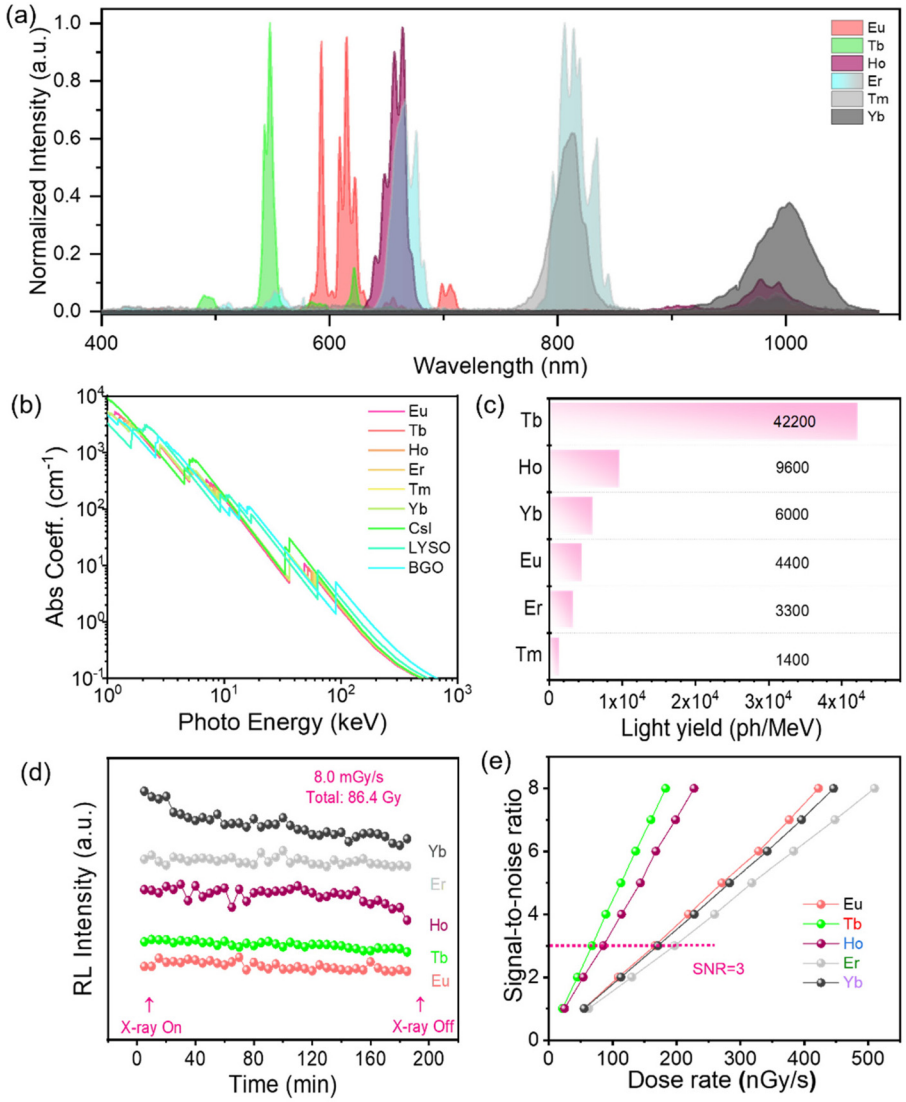

Fig. 3 (a) RL spectra of $Cs_2NaLnCl_6$ (Ln = Eu, Tb, Ho, Er, Tm, Yb). (b) Absorption coefficients of $Cs_2NaLnCl_6$ shown in (a), CsI, LYSO, and BGO as a function of X-ray energy. (c) The light yield (LY) of $Cs_2NaLnCl_6$ shown in (a). (d) The RL intensity of $Cs_2NaLnCl_6$ with an LY greater than 2000 photons per MeV under continuous X-ray irradiation at a dose rate of 8.0 mGy s^{-1} for 180 min. (e) The relationship between the signal-to-noise ratio and the dose rate of $Cs_2NaLnCl_6$ shown in (d) for the detection limit measurement.

in Table S2.† These findings highlight the potential of $Cs_2NaLnCl_6$ materials as ultrasensitive scintillators, capable of producing clear CT images even at low radiation doses, thereby minimizing human exposure to harmful radiation. These findings pave the way for the development of ultra-sensitive, next-generation indirect X-ray detectors.

2.4 Underwater X-ray imaging

$Cs_2NaLnCl_6$ materials are highly susceptible to moisture and readily degrade in humid environments, leading to the loss of their original optical properties (as shown in Fig. 4(a)). This defect greatly limits their application. Solid powders can be effectively incorporated into the polymer network structure of these composite materials. This allows polydimethylsiloxane (PDMS) to act as a protective layer for the perovskite material against moisture interference. First, we investigated the flexible characteristics of these composite films. As examples, the characteristic green and red emission of $Cs_2NaTbCl_6$ and $Cs_2NaEuCl_6$ large-area (~78 cm^2) polymer film scintillators under a UV lamp are shown in Fig. S8(a) and (b).† Their spatial resolutions, compared using a standard wire-to-plate test, are approximately 10 and 5.5 lp mm^{-1}, respectively. Transmission imaging of the seed was realized using the scintillator films (Fig. S8(b)†). Fig. S8(c)† illustrates that the flexible scintillation screens have a high degree of deformability and high toughness (the calculated tensile limit is approximately 180%). Further experiments showed that the flexible screens can mitigate the halo effect caused by uneven X-ray dose distribution in space, as shown in Fig. S8(d and e).† In addition, compared to a rigid scintillation screen, a flexible screen can

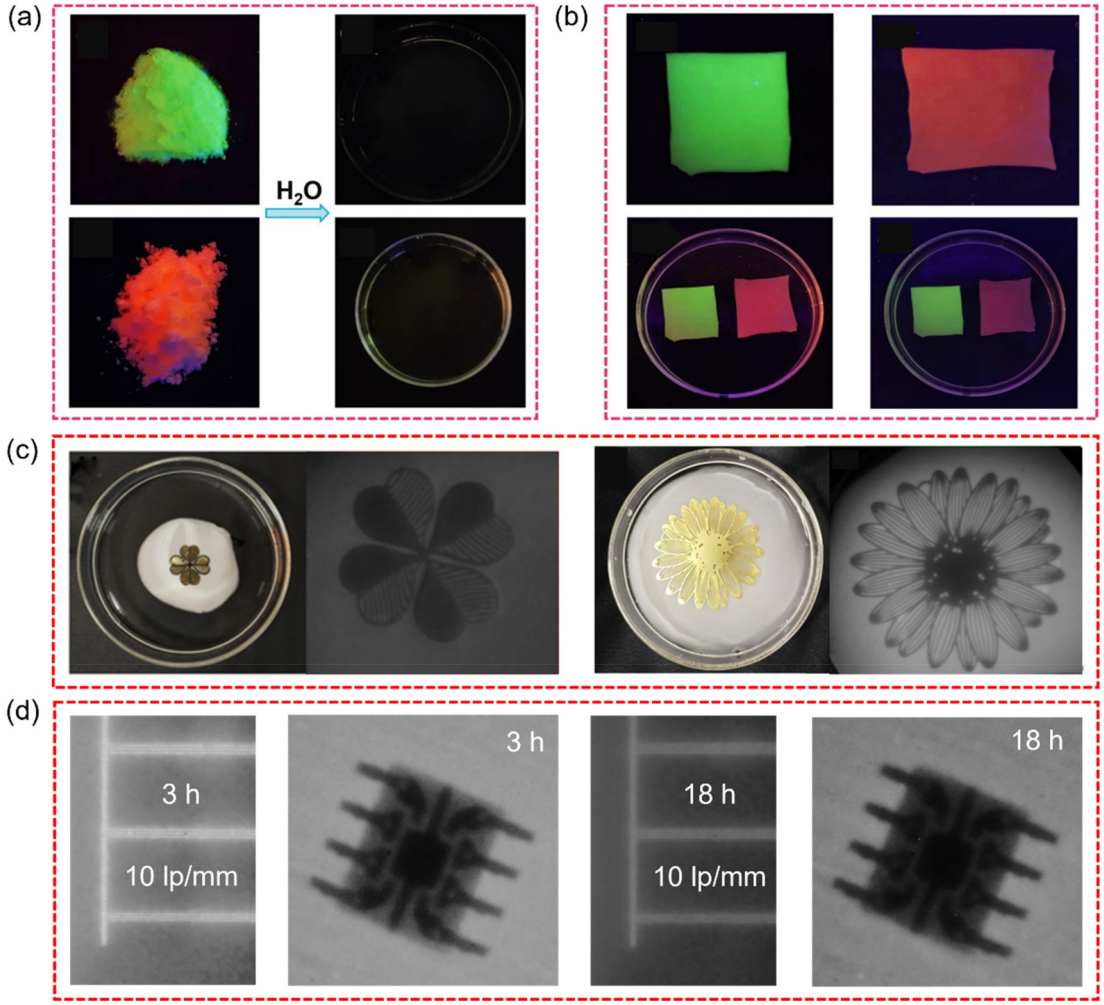

Fig. 4 (a) Fluorescence photographs of dry $Cs_2NaTb/EuCl_6$ powders (left) and (right) in water under UV. (b) Fluorescence photographs of $Cs_2NaTb/EuCl_6$@PDMS without soaking (above) and after soaking for 6 h (left bottom) and 12 h (right bottom). (c) Schematic and underwater X-ray imaging of $Cs_2NaEuCl_6$@PDMS (left) and $Cs_2NaTbCl_6$@PDMS (right). (d) Underwater X-ray imaging of $Cs_2NaTbCl_6$@PDMS for a microchip at different times.

conform to an object's surface, effectively minimizing imaging distortion and better revealing the actual shape of its internal structure, as shown in Fig. S8(f).† These investigations highlight the advantages of flexible scintillation screen imaging.

Subsequently, we investigated the waterproof properties of the flexible films and their performance in underwater X-ray imaging. As shown in Fig. 4(b), fluorescence images of $Cs_2NaTbCl_6$@PDMS and $Cs_2NaEuCl_6$@PDMS films soaked in water for 6 and 12 h demonstrate that their characteristic emission colors remain intact under UV light, indicating the polymer film's excellent water stability. These waterproof properties of the scintillators make them particularly suitable for industrial applications, such as oil field exploration. To evaluate the underwater X-ray imaging capability of $Cs_2NaLnCl_6$ films, X-ray images were captured following 2 h of water soaking. A flexible film was placed at the bottom of flat-bottomed glassware filled with deionized water, with an imaging object positioned on top. X-ray images were obtained through reflection using a prism. The results, presented in Fig. 4(c), reveal that the item outlines and shapes are clearly visible, with no notable differences compared to imaging in air. We further analyzed the stability of the underwater X-ray imaging using $Cs_2NaLnCl_6$@PDMS thin films by measuring the RL of the $Cs_2NaTbCl_6$@PDMS film immersed in water for varying durations. As shown in Fig. S9,† integrated RL intensity remains at approximately 60% of its initial value after 10 h of water soaking. It is worth noting that with more PDMS coating, the waterproof performance would be largely enhanced compared with relatively less PDMS coating (Fig. S9†). These observations highlight considerable improvement in waterproof performance following polymer coating, which is in sharp contrast to the immediate decomposition upon direct mixing of $Cs_2NaLnCl_6$ with water. The decreased RL intensity of $Cs_2NaTbCl_6$@PDMS after long-term immersion in water is due to the gradual diffusion of water through the polymer's pores. While the polymer coating effectively slows down the interaction between $Cs_2NaTbCl_6$ and water, it does not entirely prevent their contact. To demonstrate practical

application, the film was used for underwater X-ray imaging for a chip. As shown in Fig. 4(d), successful imaging was achieved at both 3 and 18 h, with a spatial resolution of 10 lp mm^{-1}. Fig. S10† further shows chip imaging at additional time points. Notably, the image captured at 3 hours is clearer than that at 18 hours due to the higher RL intensity of the film at the earlier time point (~90% of the initial value at 3 hours *versus* 40% at 18 hours). These findings provide valuable insights into addressing the instability issues associated with perovskite materials and enabling their application as scintillators under extreme conditions.

3. Conclusions

A series of Ln-MHDP polycrystals were synthesized using the solvothermal method and their structure and composition were identified. The photoluminescence properties of the samples, characterized by RE ion emission, were investigated. The samples exhibited photon emission across the entire visible and infrared spectral regions under UV and X-ray excitation. These Ln-MHDPs demonstrated excellent X-ray detection performance and irradiation stability. For instance, $Cs_2NaTbCl_6$ showed an LY of 42 200 photons per MeV under X-ray irradiation and maintained 98% of the initial RL after 180 min of continuous irradiation with a total radiation dose of about 86.4 Gy. Flexible X-ray imaging using $Cs_2NaTbCl_6$@PDMS and $Cs_2NaEuCl_6$@PDMS films achieved ideal image resolutions of 10 and 5.5 lp mm^{-1}, respectively. More importantly, the PDMS coating significantly improved the water resistance of the Ln-MHDPs, enabling clear underwater X-ray imaging. In conclusion, the demonstrated outstanding X-ray imaging performance positions Ln-MHDPs as promising scintillator materials with vast potential in multipurpose X-ray imaging applications.

Data availability

The data supporting this article have been included as part of the ESI.†

Conflicts of interest

There are no conflicts to declare.

Acknowledgements

This work was supported by the National Key R&D Program of China (2023YFB3507900 and 2022YFE0113800), the National Natural Science Foundation of China (Grant No. 22471009, 51988101, 12174016, 22122505, 22075250, and 21771161), the Beijing Natural Science Foundation (2222050) and the Beijing Nova Program (20230484350). Qingsong Hu also acknowledges the financial support from the Hubei Natural Science Foundation (2023AFB590) and Xiangyang Science and Technology Bureau (2022ABH006368). We would like to acknowledge Dr Alla Dikhtiarenko, KAUST Imaging and Characterization CoreLab. This work was supported by King Abdullah University of Science and Technology (KAUST).

References

1 Q. Chen, J. Wu, X. Ou, B. Huang, J. Almutlaq, A. A. Zhumekenov, X. Guan, S. Han, L. Liang, Z. Yi, J. Li, X. Xie, Y. Wang, Y. Li, D. Fan, D. B. L. Teh, A. H. All, O. F. Mohammed, O. M. Bakr, T. Wu, M. Bettinelli, H. Yang, W. Huang and X. Liu, All-inorganic perovskite nanocrystal scintillators, *Nature*, 2018, **561**, 88–93.

2 L. Yi, B. Hou, H. Zhao, H. Q. Tan and X. Liu, A double-tapered fibre array for pixel-dense gamma-ray imaging, *Nat. Photonics*, 2023, **17**, 494–500.

3 Y. Zhou, J. Chen, O. M. Bakr and O. F. Mohammed, Metal halide perovskites for X-ray imaging scintillators and detectors, *ACS Energy Lett.*, 2021, **6**, 739–768.

4 X. Du, S. Zhao, L. Wang, H. Wu, F. Ye, K.-H. Xue, S. Peng, J. Xia, Z. Sang, D. Zhang, Z. Xiong, Z. Zheng, L. Xu, G. Niu and J. Tang, Efficient and ultrafast organic scintillators by hot exciton manipulation, *Nat. Photonics*, 2024, **18**, 162–169.

5 J. Lu, R.-X. Qian, S.-F. Lu, S.-H. Wang, F.-K. Zheng and G.-C. Guo, High-resolution X-ray circular polarization imaging enabled by luminescent photopolymerized chiral metal-organic polymers, *Adv. Funct. Mater.*, 2024, **34**, 2410219.

6 Y. Wang, M. Li, Z. Chai, Y. Wang and S. Wang, Perovskite scintillators for improved X-ray detection and imaging, *Angew. Chem., Int. Ed.*, 2023, **62**, e202304638.

7 L.-J. Xu, X. Lin, Q. He, M. Worku and B. Ma, Highly efficient eco-friendly X-ray scintillators based on an organic manganese halide, *Nat. Commun.*, 2020, **11**, 4329.

8 W.-F. Wang, M.-J. Xie, P.-K. Wang, J. Lu, B.-Y. Li, M.-S. Wang, S.-H. Wang, F.-K. Zheng and G.-C. Guo, Thermally activated delayed fluorescence (TADF)-active coinage-metal sulfide clusters for high-resolution X-ray imaging, *Angew. Chem., Int. Ed.*, 2024, **63**, e202318026.

9 J.-X. Wang, I. Dutta, J. Yin, T. He, L. Gutiérrez-Arzaluz, O. M. Bakr, M. Eddaoudi, K.-W. Huang and O. F. Mohammed, Triplet-triplet energy-transfer-based transparent X-ray imaging scintillators, *Matter*, 2023, **6**, 217–225.

10 O. Balitskii, M. Sytnyk and W. Heiss, Recent developments in halide perovskite nanocrystals for indirect X-ray detection, *Adv. Mater. Technol.*, 2024, **9**, 2400150.

11 J.-X. Wang, L. Gutiérrez-Arzaluz, X. Wang, T. He, Y. Zhang, M. Eddaoudi, O. M. Bakr and O. F. Mohammed, Heavy-atom engineering of thermally activated delayed fluorophores for high-performance X-ray imaging scintillators, *Nat. Photonics*, 2022, **16**, 869–875.

12 W. Ma, T. Jiang, Z. Yang, H. Zhang, Y. Su, Z. Chen, X. Chen, Y. Ma, W. Zhu, X. Yu, H. Zhu, J. Qiu, X. Liu, X. Xu

and Y. M. Yang, Highly resolved and robust dynamic X-ray imaging using perovskite glass-ceramic scintillator with reduced light scattering, *Adv. Sci.*, 2021, **8**, e2003728.

13 J. Li, Q. Hu, J. Xiao and Z. G. Yan, High-stability double perovskite scintillator for flexible X-ray imaging, *J. Colloid Interface Sci.*, 2024, **671**, 725–731.

14 Y. Wang, C. Wang, L. Men, Q. Hu and J. Xiao, Colloidal synthesis of hollow double perovskite nanocrystals and their applications in X-ray imaging, *Inorg. Chem.*, 2024, **63**, 5734–5742.

15 Q. Fan, Y. Ma, H. Xu, Y. Song, Y. Liu, J. Luo and Z. Sun, Near-room-temperature reversible switching of quadratic optical nonlinearities in a one-dimensional perovskite-like hybrid, *Microstructures*, 2022, **2**, 2022013.

16 R.-X. Qian, J. Lu, M. Cui, S.-H. Wang, P.-K. Wang, B.-Y. Li, F.-K. Zheng and G.-C. Guo, High-resolution X-ray imaging with 0D organic–metal halide scintillator featuring reversed exciton trapping, *Laser Photonics Rev.*, 2025, **19**, 2401342.

17 A. Jana, S. Cho, S. A. Patil, A. Meena, Y. Jo, V. G. Sree, Y. Park, H. Kim, H. Im and R. A. Taylor, Perovskite: scintillators, direct detectors, and X-ray imagers, *Mater. Today*, 2022, **55**, 110–136.

18 B. Wang, X. Yang, S. Chen, S. Lu, S. Zhao, Q. Qian, W. Cai, S. Wang and Z. Zang, Flexible perovskite scintillators and detectors for X-ray detection, *iScience*, 2022, **25**, 105593.

19 Y. Zhou, X. Wang, T. He, H. Yang, C. Yang, B. Shao, L. Gutiérrez-Arzaluz, O. M. Bakr, Y. Zhang and O. F. Mohammed, Large-area perovskite-related copper halide film for high-resolution flexible X-ray imaging scintillation screens, *ACS Energy Lett.*, 2022, **7**, 844–846.

20 Y. Ling, X. Zhao, P. Hao, Y. Song, J. Liu, L. Zhao, Y. Qian and C. Guo, Gd^{3+}-sensitized rare earth fluoride scintillators for high-resolution flexible X-ray imaging, *Chem. Eng. J.*, 2023, **476**, 146790.

21 X. Ou, X. Qin, B. Huang, J. Zan, Q. Wu, Z. Hong, L. Xie, H. Bian, Z. Yi, X. Chen, Y. Wu, X. Song, J. Li, Q. Chen, H. Yang and X. Liu, High-resolution X-ray luminescence extension imaging, *Nature*, 2021, **590**, 410–415.

22 J. Zhao, L. Zhao, Y. Deng, X. Xiao, Z. Ni, S. Xu and J. Huang, Perovskite-filled membranes for flexible and large-area direct-conversion X-ray detector arrays, *Nat. Photonics*, 2020, **14**, 612–617.

23 H. Zhang and H. Zhang, Special issue: rare earth luminescent materials, *Light: Sci. Appl.*, 2022, **11**, 260.

24 S. Li, L. Zhou and H. Zhang, Investigation progresses of rare earth complexes as emitters or sensitizers in organic light-emitting diodes, *Light: Sci. Appl.*, 2022, **11**, 177.

25 R. F. Muniz, V. S. Zanuto, M. S. Gibin, J. V. Gunha, A. Novatski, J. H. Rohling, A. N. Medina and M. L. Baesso, Down- and up-conversion processes in Nd^{3+}/Yb^{3+} co-doped sodium calcium silicate glasses with concomitant Yb^{2+} assessment, *J. Rare Earths*, 2023, **41**, 342–348.

26 V. Naresh, P.-R. Cha and N. Lee, $Cs_2NaGdCl_6:Tb^{3+}$—A highly luminescent rare-earth double perovskite scintillator for low-dose X-ray detection and imaging, *ACS Appl. Mater. Interfaces*, 2024, **16**, 19068–19080.

27 V. Vaněček, K. Děcká, E. Mihóková, V. Čuba, R. Král and M. Nikl, Advanced halide scintillators: from the bulk to nano, *Adv. Photonics Res.*, 2022, **3**, 2200011.

28 V. Retivov, V. Dubov, D. Kuznetsova, A. Ismagulov and M. Korzhik, Gd^{3+} content optimization for mastering high light yield and fast $Gd_xAl_2Ga_3O_{12}:Ce^{3+}$ scintillation ceramics, *J. Rare Earths*, 2023, **41**, 1911–1918.

29 L. Sun, B. Dong, J. Sun, Y. Wang, R. Sun, S. Hu, B. Zhou, W. Xu, X. Bai, L. Xu, D. Zhou and H. Song, Fabrication, optical property, and white LED application of novel lanthanide–based family Cs_2NaLnX_6 (X = Cl, Br, I) perovskite nanomaterials, *Laser Photonics Rev.*, 2023, **17**, 2300045.

30 Y. Chen, S. Liu, N. Zhou, N. Li, H. Zhou, L.-D. Sun and C.-H. Yan, An overview of rare earth coupled lead halide perovskite and its application in photovoltaics and light emitting devices, *Prog. Mater. Sci.*, 2021, **120**, 100737.

31 Z. Rao, X. Zhao and X. Gong, Rare-earth-based lead-free halide double perovskites for light emission: recent advances and applications, *Adv. Funct. Mater.*, 2024, **34**, 2406424.

32 Y. Li, Q. Yang, H. Li, X. Fu, H. Yue, Z. Li, J. Feng and H. Zhang, Rare earth-based $Cs_2NaRECl_6$ (RE = Tb, Eu) halide double perovskite nanocrystals with multicolor emissions for anticounterfeiting and LED applications, *J. Mater. Chem. C*, 2024, **12**, 11778–11784.

33 T. Wang, G. Liu and Z. Xia, Chemical unit co-substitution enabling broadband and tunable near-infrared emission in garnet-type $Lu_3Sc_2Ga_3O_{12}$: Cr^{3+} phosphors, *Microstructures*, 2022, **2**, 19.

34 Q. Hu, Z. Pan and G. Liang, Site occupation and energy transfer in full color emitting phosphor $Ba_2Ca(BO_3)_2$: $Ce^{3+}(K^+)$,Eu^{2+},Mn^{2+}, *J. Rare Earths*, 2022, **40**, 1691–1698.

35 Qingsong Hu, Deng Zhenzhou, Manchen Hu, Anjiang Zhao and Yaqi Zhang, X-ray scintillation in lead-free double perovskite crystals, *Sci. China:Chem.*, 2018, **61**, 1581–1586.

36 R. I. López-Esquivel, I. A. Garduño-Wilches, J. C. Guzmán-Olguín, T. Rivera Montalvo and J. Guzmán-Mendoza, Thermally coupled energy levels of Eu^{3+} within the $BaHfO_3$ matrix, excited with UV radiation, *Appl. Radiat. Isot.*, 2022, **186**, 110266.

37 P. Saghy, A. M. Brown, C. Chu, L. C. Dube, W. Zheng, J. R. Robinson and O. Chen, Lanthanide double perovskite nanocrystals with emissions covering the UV–C to NIR spectral range, *Adv. Opt. Mater.*, 2023, **11**, 2300277.

38 Y. Wang, P. Dang, L. Qiu, G. Zhang, D. Liu, Y. Wei, H. Lian, G. Li, Z. Cheng and J. Lin, Multimode luminescence tailoring and improvement of $Cs_2NaHoCl_6$ cryolite crystals via Sb^{3+}/Yb^{3+} alloying for versatile photoelectric applications, *Angew. Chem., Int. Ed.*, 2023, **62**, e202311699.

39 L. Guo, Y. Wang, J. Zhang, Y. Wang and P. Dong, Near-infrared quantum cutting in Ho^{3+}, Yb^{3+}-codoped $BaGdF_5$ nanoparticles via first-and second-order energy transfers, *Nanoscale Res. Lett.*, 2012, **7**, 636.

40 G. Zhang, P. Dang, L. Tian, W. Yang, Z. Cheng, H. Lian and J. Lin, Boosting energy transfer from self-trapped exciton to

Er^{3+} through Sb^{3+} doping in $Cs_2Na(Lu/Er)Cl_6$ double perovskites, *Adv. Opt. Mater.*, 2023, **11**, 2202369.

41 G. Pan, X. Bai, D. Yang, X. Chen, P. Jing, S. Qu, L. Zhang, D. Zhou, J. Zhu, W. Xu, B. Dong and H. Song, Doping lanthanide into perovskite nanocrystals: highly improved and expanded optical properties, *Nano Lett.*, 2017, **17**, 8005–8011.

42 X. Hong, L. Zhang, S. Xu, Z. Cheng, Y. Wang, B. A. Goodman, D. Xiong and W. Deng, White light luminescence in Dy/Tm co-doped yttria stabilized zirconia single crystals, *J. Rare Earths*, 2023, **41**, 1904–1910.

43 L. Li, F. Xing, X. Zhang, H. Hao and Y. Wang, Emission enhancement and color modulation of Tm(Ho)/Yb codoped $Gd_2(MoO_4)_3$ thin films via the use of multilayered structure, *J. Rare Earths*, 2021, **39**, 765–771.

44 T. Cai, J. Wang, W. Li, K. Hills-Kimball, H. Yang, Y. Nagaoka, Y. Yuan, R. Zia and O. Chen, Mn^{2+}/Yb^{3+} codoped $CsPbCl_3$ perovskite nanocrystals with triple-wavelength emission for luminescent solar concentrators, *Adv. Sci.*, 2020, **7**, 2001317.

45 Y. Wang, X. Yin, W. Liu, J. Xie, J. Chen, M. A. Silver, D. Sheng, L. Chen, J. Diwu, N. Liu, Z. Chai, T. E. Albrecht-Schmitt and S. Wang, Emergence of uranium as a distinct metal center for building intrinsic X-ray scintillators, *Angew. Chem., Int. Ed.*, 2018, **57**, 7883–7887.

46 Z. Zeng, B. Huang, X. Wang, L. Lu, Q. Lu, M. Sun, T. Wu, T. Ma, J. Xu, Y. Xu, S. Wang, Y. Du and C.-H. Yan, Multimodal luminescent $Yb^{3+}/Er^{3+}/Bi^{3+}$-doped perovskite single crystals for X-ray detection and anti-counterfeiting, *Adv. Mater.*, 2020, **32**, 2004506.